Ultrasound viscoelasticity assessment using an adaptive torsional shear wave propagation method

Abderrahmane Ouared
Laboratory of Biorheology and Medical Ultrasonics, University of Montréal Hospital Research Center (CRCHUM), Montréal, Québec H2X 0A9, Canada and Institute of Biomedical Engineering, University of Montréal, Montréal, Québec H3T 1J4, Canada

Siavash Kazemirad and Emmanuel Montagnon[a)]
Laboratory of Biorheology and Medical Ultrasonics, University of Montréal Hospital Research Center (CRCHUM), Montréal, Québec H2X 0A9, Canada

Guy Cloutier[b)]
Laboratory of Biorheology and Medical Ultrasonics, University of Montréal Hospital Research Center (CRCHUM), Montréal, Québec H2X 0A9, Canada; Department of Radiology, Radio-Oncology and Nuclear Medicine, University of Montréal, Montréal, Québec H3T 1J4, Canada; and Institute of Biomedical Engineering, University of Montréal, Montréal, Québec H3T 1J4, Canada

(Received 2 June 2015; revised 2 February 2016; accepted for publication 15 February 2016; published 7 March 2016)

Purpose: Different approaches have been used in dynamic elastography to assess mechanical properties of biological tissues. Most techniques are based on a simple inversion based on the measurement of the shear wave speed to assess elasticity, whereas some recent strategies use more elaborated analytical or finite element method (FEM) models. In this study, a new method is proposed for the quantification of both shear storage and loss moduli of confined lesions, in the context of breast imaging, using adaptive torsional shear waves (ATSWs) generated remotely with radiation pressure.
Methods: A FEM model was developed to solve the inverse wave propagation problem and obtain viscoelastic properties of interrogated media. The inverse problem was formulated and solved in the frequency domain and its robustness to noise and geometric constraints was evaluated. The proposed model was validated *in vitro* with two independent rheology methods on several homogeneous and heterogeneous breast tissue-mimicking phantoms over a broad range of frequencies (up to 400 Hz).
Results: Viscoelastic properties matched benchmark rheology methods with discrepancies of 8%–38% for the shear modulus G' and 9%–67% for the loss modulus G''. The robustness study indicated good estimations of storage and loss moduli (maximum mean errors of 19% on G' and 32% on G'') for signal-to-noise ratios between 19.5 and 8.5 dB. Larger errors were noticed in the case of biases in lesion dimension and position.
Conclusions: The ATSW method revealed that it is possible to estimate the viscoelasticity of biological tissues with torsional shear waves when small biases in lesion geometry exist. © *2016 American Association of Physicists in Medicine.* [http://dx.doi.org/10.1118/1.4942813]

Key words: dynamic elastography, mechanical characterization, viscoelastic properties, breast cancer, ultrasound imaging, adaptive torsional shear wave elastography, shear wave elastography

1. INTRODUCTION

In dynamic elastography, shear waves can be generated mechanically by an external vibration source or remotely using acoustic radiation force. The type of shear waves generated depends on the source of excitation. For example, the sonoelasticity method[1,2] uses two sources of vibration slightly shifted in frequency, where interferences give rise to quasi-stationary crawling waves. The low velocity of these waves allows their detection by the conventional Doppler ultrasound method.[3] Subsequently, the Young's (elasticity) modulus E is determined with measured shear wave velocity ($E \approx 3\mu$ and $\mu = \rho v_s^2$, where μ is the shear modulus, ρ the density of the medium, and v_s the shear wave speed).[1] In Ref. 4, a confocal ultrasound transducer is used to generate a radiation pressure in the kHz range in a medium by firing the central and annular elements of the probe at different frequencies. In other studies, harmonic and/or transient shear waves were generated by a rigid interface coupled to a shaker positioned on the surface of the probed medium.[5–7] Plane shear waves were produced by a vibrating plate.[6] Cylindrical shear wavefronts were also generated mechanically by a vibrating needle.[8,9] A torsional shear wave propagation approach was first introduced in the context of dynamic elastography in Ref. 10. Torsional shear waves were generated mechanically by a semispherical cup positioned on the surface of the breast of a women volunteer.[10] In all the abovementioned studies, mechanical properties were estimated through analytical or numerical solution of an inverse wave propagation problem.

The main drawbacks of external excitation techniques are the complex displacement field that may be generated, the vibration-induced probe motion artifacts, and the necessity of using an external bulky device to produce vibrations. To overcome some of these limitations, a remote palpation technique using acoustic radiation force to produce *in situ* vibrations was developed.[11] Today, the most common remote technologies used clinically are acoustic radiation force impulse (ARFI)[12,13] and supersonic shear imaging (SSI)[14] methods. In ARFI, semicylindrical shear waves are produced, whereas quasiplane wavefronts obtained by the superposition of semicylindrical shear waves are generated in SSI. Mechanical properties can be quantified either from the shear wave group velocity measured by the time of flight method[14,15] or the phase shift method.[16]

As in the case of external vibrating methods, remote palpation techniques also suffer from strong attenuation of the shear wave amplitude with propagation on a few millimeters, which can affect the signal-to-noise ratio (SNR) and the biological tissue characterization accuracy, especially at high frequencies. Another limitation of some remote palpation techniques is that they only allow estimating elasticity.[14,17] Viscosity assessment may thus be of value knowing that some benign and malignant lesions have similar elasticity moduli.[18] A few remote palpation techniques have recently been developed to simultaneously estimate elasticity and viscosity.[19–21] A common approach is to measure the shear wave velocity at different frequencies and to estimate the viscosity by fitting the experimental data to a rheological model.[22,23] Alternatively, the viscosity can be obtained via analytical or numerical solutions of an inverse wave propagation problem.[24,25]

The aim of this study was to propose a method based on adaptive torsional shear waves (ATSWs) generated remotely to assess viscoelastic properties (elasticity and viscosity) in the context of breast imaging. A finite element method (FEM) was used to quantify mechanical properties through the numerical solution of an inverse problem based on an ATSW propagation model. For evaluation, breast imaging-reporting and data system (BI-RADS) 3 and 4 lesion mimicking phantoms were fabricated and tested. We specifically tested circular inclusions with clear margin and a diameter typical of nonpalpable lesions. Mechanical properties were compared to two independent benchmark methods over a broad range of frequencies to evaluate the accuracy of the proposed ATSW technique.

2. MATERIALS AND METHODS

2.A. Phantom fabrication

As the viscoelastic properties of breast tissues and lesions can be very different depending on several parameters such as the cellular composition, the age of the patient, the menstrual cycle, the hormonal status, and the ethnicity,[15,18,26–28] we fabricated five tissue-mimicking phantoms covering a large range of viscoelasticity values. Among these phantoms, three were homogeneous (phantoms #1–#3) and two were heterogeneous (phantoms #4 and #5) with a cylindrical inclusion at their center (radius $R = 5$ mm). For phantom #4, the inclusion was softer than the surrounding medium, whereas it was stiffer in the case of phantom #5. As the viscoelasticity of breast lesions also depends on the type of disease and its stage of maturity, lesions can be softer or stiffer than the surrounding parenchyma.[15,26,29] The goal of these configurations (soft-stiff and stiff-soft) was to simulate different viscoelasticity contrasts between lesions and their surrounding medium. All phantoms had the same volume (1000 cm^3) and were made with agar (product No. A 9799, Sigma-Aldrich chemical, St. Louis, MO, USA) and gelatin (product No. G 2500, Sigma-Aldrich chemical) at different concentrations following the protocol of Ref. 30. Samples were taken from each phantom gel mixture to estimate viscoelastic properties using two benchmark methods described next. Table I summarizes details on concentrations used for each phantom. Percentages are in proportion of the water weight.

2.B. Benchmark rheology methods

Two rheology methods were chosen to validate ATSW viscoelasticity results. The Winsorized mean (WM) of those results (calculated relative to the number of repeated measures) was used as the final data set for comparisons.

2.B.1. Longitudinal wave propagation method (LWPM)

Following the same protocol and experimental setup of Ref. 31, two rod-shaped samples with a square cross section of 5 mm were fabricated from each agar-gelatin mixture of phantom inclusions and surrounding media. Samples were attached to an accelerometer (#320C33, PCB, Depew, NY, USA), which was itself connected to a shaker (Type 4810, Bruel and Kjær, Nærum, Denmark). Longitudinal waves at different frequencies (40–400 Hz with steps of 40 Hz) were generated by harmonic excitation in the sample by the shaker. Velocities of both sample ends were measured by the accelerometer and a laser Doppler vibrometer, respectively. For each sample, measurements were repeated three times. The complex elastic modulus was determined from measured complex wavenumbers, which were assessed using a transfer function method between velocities at both ends.[32] This method was not used for the characterization of phantom #1 and the inclusion of phantom #4, as those samples were too soft and could not be attached to the shaker.

2.B.2. Hyperfrequency viscoelastic spectroscopy (HFVS)

The second method used for the evaluation of the ATSW technique was hyperfrequency viscoelastic spectroscopy.[33]

TABLE I. Agar and gelatin concentrations used for the fabrication of each phantom. Proportions are relative to the water weight.

Phantom	#1	#2	#3	#4	#5
Surrounding (agar-gelatin) (%)	4–3	5–4	6–5	5–4	5–4
Inclusion (agar-gelatin) (%)	N/A	N/A	N/A	4–3	5–5

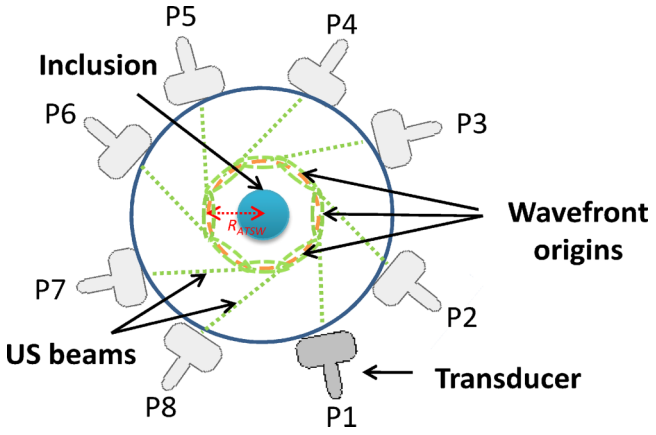

FIG. 1. Schematic representation of the mechanical rotation of the ultrasound transducer around the phantom from position 1 ($P1$) to position 8 ($P8$) used to reconstruct torsional shear wave propagation.

Cylindrical samples (diameter of 10 mm) were prepared from the same gel mixtures and analyzed with the RheoSpectris instrument (Model C-400, Rheolution, Inc., Montreal, QC, Canada). The complex shear modulus was measured between 40 and 400 Hz (steps of 40 Hz) and repeated six times for each sample.

2.C. Adaptive torsional shear wave generation

To mimic the generation of torsional waves according to the theoretical concept of the octagonal probe introduced in Ref. 34, eight different quasiplane shear wavefronts were generated using a frequency-adapted radiation force[35] by moving the ultrasound transducer around the phantom, as in Ref. 36. Shear wavefronts were then combined linearly to form a closed path (see Fig. 1). The combination was done in postprocessing under the assumption of the superposition principle,[37] as detailed in Ref. 36. The transducer was mechanically rotated around phantoms at locations $P1$–$P8$ using a 3D positioner.

The radiation force was remotely generated by short impulse excitations using a linear array transducer (ATL L7-4, Philips, Bothell, WA, USA) controlled by a Verasonics system (V1, Verasonics, Inc., Redmond, WA, USA). To generate each quasiplane wavefront, a home implantation of supersonic beam sequences similar to SSI was used. Each wavefront was produced by three focused pushes, each one being generated at its optimal frequency.[35] The transducer excitation voltage was 30 V and the focused push duration was maintained around 100 μs at all frequencies used for the generation of the radiation force. Immediately after the radiation pressure pushing phase, the tracking of shear waves (imaging phase) was performed by the same probe using ultrafast plane wave imaging at a frame rate of 2 kHz during around 10 ms.[14] The estimation of displacements generated by quasiplane shear waves was performed using a one-dimensional (1D) normalized cross-correlation algorithm implemented on graphics processing unit (GPU).[38] The reconstruction of the circular ATSW field with a radius $R_{ATSW} = 20$ mm (see Figs. 1 and 2) was performed in the time domain by the combination of quasiplane displacement fields using a dedicated algorithm.[36] Stationary displacement maps (SDMs) at different frequencies were also calculated using the Fourier transform of the temporal displacement field, as in Ref. 36. This experimental protocol was repeated three times for each phantom and average results at each frequency are presented.

2.D. Estimation of viscoelastic parameters

The estimation of the viscoelasticity was performed in two steps. First, the 2D FEM model provided displacement profiles related to the shear storage and loss moduli at each frequency between 40 and 400 Hz (steps of 40 Hz). The simulated profiles were compared to the experimental ones at each frequency to

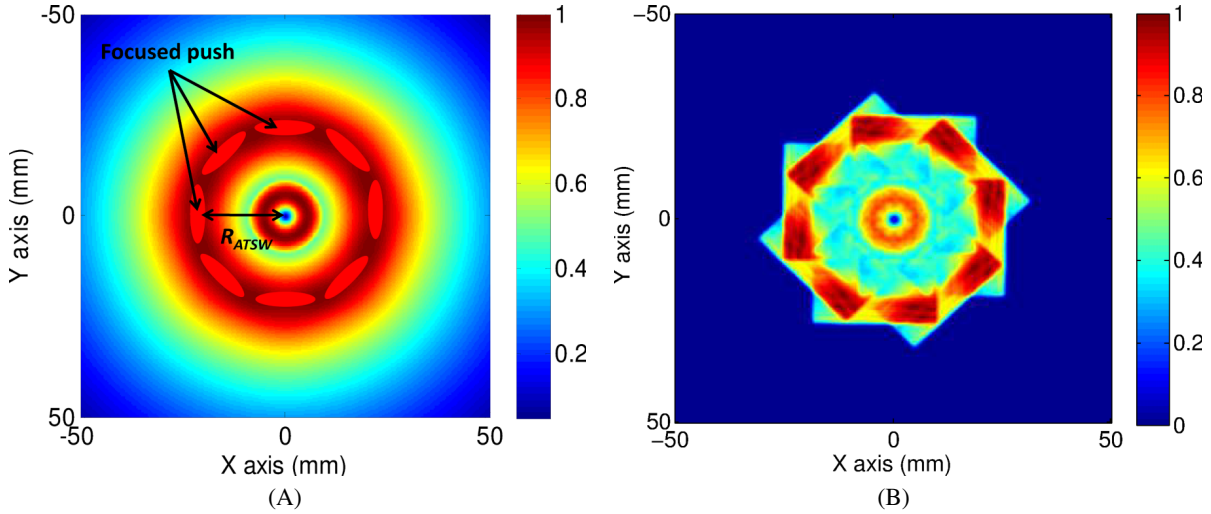

FIG. 2. SDM of the finite element method simulated ATSW front for phantom #3 (A) and experimental SDM (B) at 120 Hz. The black arrow represents the propagation distance from the focused push located on the left side of the image toward the center of the circular ATSW field. SDM maps were normalized to the amplitude of the maximum displacement at focused push locations.

find the best matching using a minimization method. Once the two profiles (simulated and experimental) were matched, the inverse problem provided the experimental values of the shear storage and loss moduli.

2.E. Finite element method simulation

The propagation of adaptive torsional shear waves was simulated by the finite element method (COMSOL, Inc., ver. a3.5, Burlington, MA, USA). All FEM simulations were performed in the frequency domain to compute the displacement field at specific frequencies (between 40 and 400 Hz with a step of 40 Hz). The FEM model was used to solve the Navier differential equation that links the displacement field to mechanical properties of the medium.[39,40] By omitting the time dependent term of displacements, $e^{i\omega t}$, the Navier equation is expressed as

$$(\lambda+2G)\nabla(\nabla\cdot\mathbf{U})+G\nabla^2\mathbf{U}=\rho\left(\frac{\partial^2\mathbf{U}}{\partial t^2}\right), \quad (1)$$

where λ, G, $\mathbf{U}(x,y)$, and ρ are the first Lamé coefficient, the complex shear modulus, the displacement, and the density (assumed to be similar to the water density of 1080 kg/m^3), respectively. As all terms of this equation are known except the complex shear modulus, its resolution allows the determination of G.

ATSW with $R_{\mathrm{ATSW}}=20$ mm was simulated by imposing a transient displacement (impulse excitation) at each mesh node contained within the area of ultrasound focused pushes, which was considered as an ellipse with major and minor diameters of 20 and 5 mm, respectively (as observed experimentally). To simulate homogeneous phantoms #1–#3, the spatial distribution of the complex shear modulus $G=G'+iG''$, where G' and G'' are the shear storage and shear loss moduli, was assumed to be uniform in the propagation medium. This latter was modeled as a square region (200×200 mm^2) surrounded by artificial absorbers (at all boundaries) to avoid undesirable wave reflections. Absorbers were simulated as layers with similar storage modulus as the propagation medium to ensure the continuity of the mechanical impedance, and with a shear loss modulus increasing exponentially with layer thicknesses. The thickness of absorbers was arbitrary defined as two times the wavelengths.

In the case of heterogeneous phantoms #4 and #5, a centered 5 mm radius circular inclusion embedded in the surrounding medium was defined by considering a different spatial distribution of the complex shear modulus. For each stationary displacement field investigated, an adapted extra fine mesh element size was used to have at least four nodes per wavelength. For the initialization of the FEM model, some *a priori* known parameters were required, such as starting values of the shear storage and loss moduli (determined from benchmark methods), and the search range. Furthermore, in the case of heterogeneous phantoms, geometrical parameters as the shape and size of the heterogeneity, and its location were considered in the FEM model. Materials constituting propagation media (homogeneous phantoms and inclusions, and surrounding media for heterogeneous phantoms) were assumed to be linear and isotropic.

2.F. Forward and inverse problem formulation

A parametric approach based on nonlinear least squares optimization was used to formulate the inverse problem. The minimization was performed between simulated and experimental displacement profiles along the black arrow of Fig. 2 (i.e., between the most left-sided focused push to the center of the circular torsional shear wavefront). Due to the axial symmetry of the problem, any radial path could have been used for minimization. The cost function was defined as

$$G_{\mathrm{medium}}\ \mathrm{or}\ \left(G_{\mathrm{inclusion}},G_{\mathrm{surrounding}}\right) = \arg\min\left\{\left|\mathrm{Amp}[U^s]-\mathrm{Amp}[U^E]\right|^2\right\}, \quad (2)$$

where G is the shear modulus and Amp is the amplitude of FEM simulated (U^S) and experimental (U^E) displacements. Stationary displacement fields were obtained at different frequencies, and the optimization allowed retrieving G'_{medium} and G''_{medium} for homogeneous phantoms, and $G'_{\mathrm{inculsion}}$, $G''_{\mathrm{inclusion}}$, $G'_{\mathrm{surrounding}}$, and $G''_{\mathrm{surrounding}}$ in the case of heterogeneous phantoms. Before using the inverse problem to assess the viscoelastic parameter, the forward problem was validated using results provided by benchmark methods.

2.G. Robustness of the inverse problem to assess *G′* and *G″*

The inverse problem was evaluated by adding zero-mean random noise, at SNR from 19.5 to 8.5 dB, to experimental displacement fields. Reported biases on G' and G'' were averaged over three measurements with ten different additions of noise within the bandwidth of 40 to 400 Hz (steps of 40 Hz). In the case of heterogeneous phantoms, the impact of geometrical *a priori* (size and position of the inclusion) on estimated mechanical properties was also evaluated. Errors on parameter $X(f)$, where $X(f)$ is either the storage or the loss modulus depending on frequency (f), were computed as

$$\mathrm{Error}\ (\%)=\frac{X_{\mathrm{estimated}}(f)-X_{\mathrm{reference}}(f)}{X_{\mathrm{reference}}(f)}\times100, \quad (3)$$

where the subscript reference corresponds to the Winsorized mean of benchmark rheology methods (LWPM and HFVS) at each frequency. For each SNR value or geometrical variation (radius, X-axis, and Y-axis shifts) in the case of heterogeneous phantoms, the error was estimated at each frequency and the mean and standard deviation (SD) values from the ten frequency samples were presented.

3. RESULTS

3.A. Forward problem validation

The forward problem was validated with the dataset of the homogeneous phantom #3 and heterogeneous phantoms #4

and #5. The choice of the third phantom for the homogeneous case was arbitrary. Figure 2 shows a typical simulated stationary displacement field at 120 Hz in the homogeneous case. The black arrow represents the propagation distance from the left-sided focused push toward the center of the circular ATSW field. Figures 3(A)–3(C) present simulated and experimental displacement profiles at 120 Hz over the black arrow propagation path of Fig. 2 for phantoms #3–#5, respectively. As mentioned previously, the Winsorized mean of viscoelastic properties of agar-gelatin gels between 40 and 400 Hz (surrounding media and inclusions) obtained with benchmark LWPM and HFVS methods was used in FEM simulations. LWPM and HFVS viscoelasticity results are presented in Table II for homogeneous phantoms and Table III for heterogeneous ones (see the Appendix).

Correlation coefficients (R) between simulated and experimental profiles, exemplified at 120 Hz in Fig. 3, were between 0.95 and 0.76 for the homogeneous phantom #3, between 0.89 and 0.72 for the heterogeneous phantom #4 with a soft inclusion, and between 0.91 and 0.72 for the heterogeneous phantom #5 with a stiff inclusion, over the bandwidth of 40 to 400 Hz. Because similar correlation ranges were obtained for all phantoms, one can conclude that the presence of an inclusion did not affect the validity of the forward problem.

3.B. Robustness of the inverse problem

Figure 4 illustrates the impact of the SNR on the estimation of viscoelastic properties in phantom #3. Mean errors were between 16% and 19%, with SDs between 2% and 8% for the shear storage modulus, and between 20% and 32% (SDs between 3% and 18%) for the shear loss modulus at SNRs of 19.5 to 8.5 dB.

In the case of heterogeneous phantoms, Figs. 5(A) and 6(A) show the effect of a bias between ±20% of the inclusion radius on viscoelasticity assessments of phantoms #4 and #5, respectively. Errors on storage moduli were less than 16% (phantom #4) and 28% (phantom #5) for surrounding media, and up to 30% (phantom #4) and 42% (phantom #5) for inclusions. For phantom #4, errors on loss moduli of the surrounding medium were in the same range as for the shear moduli (up to 39%) for radius variations between ±15%, and higher for larger radius variations. For the soft inclusion of that phantom, errors were much higher and reached 319%. In the case of phantom #5, errors on loss moduli were higher for both the surrounding medium (80%–208%) and the inclusion (35%–238%).

Figures 5(B), 5(C), 6(B), and 6(C) illustrate viscoelasticity errors in phantoms #4 and #5, respectively, for an inclusion shift of ±20% of its radius in X- and Y-directions. Errors on storage moduli of surrounding media were less than 21% (phantom #4) and less than 25% (phantom # 5) for the X-direction shift, and up to 24% for both phantoms for a shift in the Y-direction. However, as it was the case for a bias on radius assessment of the inclusion, errors on loss moduli of surrounding media were higher for both phantoms. Errors reached 132% (X-direction shift) and 115% (Y-direction shift) for

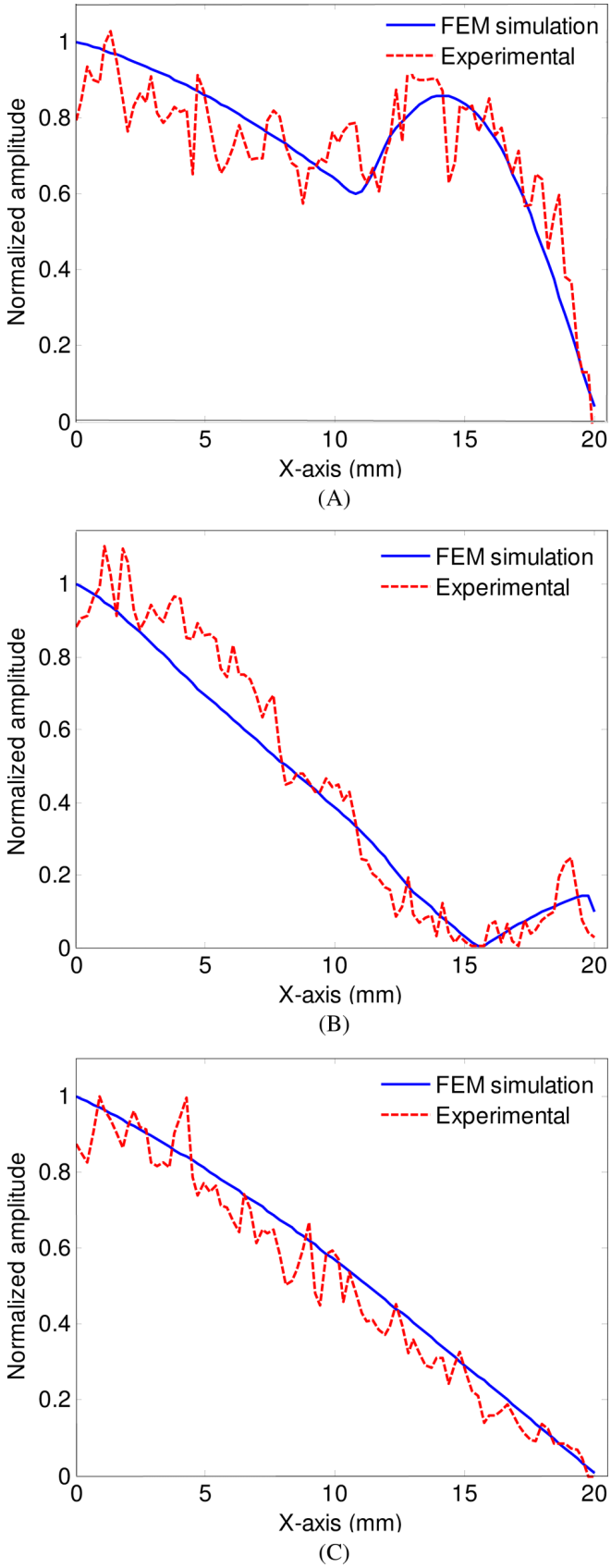

FIG. 3. Comparison between normalized displacement amplitudes obtained from FEM simulations (solid line) and experimental measurements (dashed line) in (A) the homogeneous phantom #3, (B) the heterogeneous phantom with a soft inclusion (phantom #4), and (C) the heterogeneous phantom with a stiff inclusion (phantom #5) at 120 Hz.

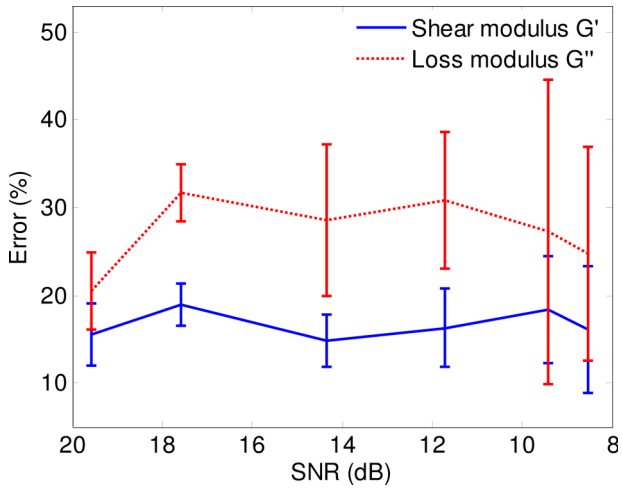

FIG. 4. Errors between predicted finite element method and experimental shear storage (solid blue) and loss (dashed red) moduli versus SNR in phantom #3. For each SNR (between 19.5 and 8.5 dB), the error was computed in the frequency range between 40 and 400 Hz. Results are means and standard deviations obtained from ten frequency samples.

phantom #4 and varied between 80% and 202% (X-direction shift) and were less than 192% (Y-direction shift) for phantom #5. In the case of the soft inclusion (phantom #4), errors on storage moduli were below 32% (X-direction shift) and below 50% (Y-direction shift). For loss moduli, errors were again higher with a maximum at 135% for the X-direction shift and 165% for the Y-direction shift. For the stiff inclusion (phantom #5), reported errors are in the same ranges. For the storage modulus errors were below 73% (X-direction shift) and below 75% (Y-direction shift), whereas they were between 35% and 138% (X-direction shift) and up to 172% (Y-direction shift) for loss moduli.

3.C. Assessment of viscoelasticity measurements

All phantoms were considered for the validation of the inverse problem solution. Figure 7 shows comparisons between shear storage and shear loss moduli for homogeneous phantoms compared with benchmark rheology results. As mentioned previously, benchmark results correspond to Winsorized means and standard deviations at each frequency of LWPM (three measurements) and HFVS (six measurements) methods (total of nine samples at each frequency). For the softest phantom [Fig. 7(A)], the frequency-dependent rheology behavior of the shear storage modulus differed between the proposed method (ATSW) and benchmark measures (HFVS only in this case, see Table II). However, G' values were in agreement between both methods at frequencies of 80 to 280 Hz with discrepancies [computed with Eq. (3)] smaller than 20%. For the shear loss modulus, discrepancies were smaller than 42% for the whole frequency range. For the second phantom [Fig. 7(B)], differences between ATSW and benchmark results were between 8% and 15% for the storage modulus, and between 9% and 31% for the loss modulus over the whole frequency range. For the stiffest phantom [Fig. 7(C)], discrepancies were smaller than 6% for the storage

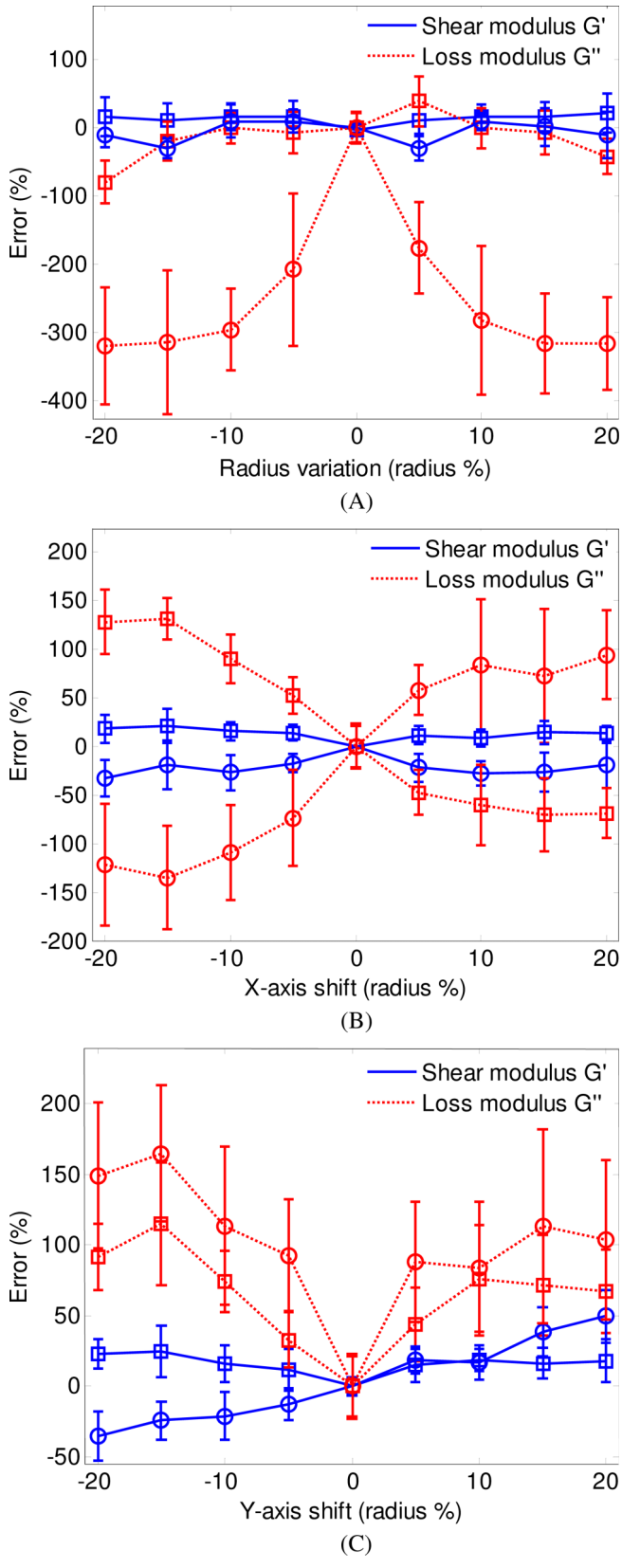

FIG. 5. Errors between predicted finite element method and experimental shear storage (solid blue) and loss (dashed red) moduli for the surrounding medium (squares) and the inclusion (circles) versus (A) the inclusion radius variation, (B) the X-direction shift of the inclusion, and (C) the Y-direction shift of the inclusion in phantom #4. Errors were computed in the frequency range between 40 and 400 Hz. Results are means and standard deviations obtained from ten frequency samples.

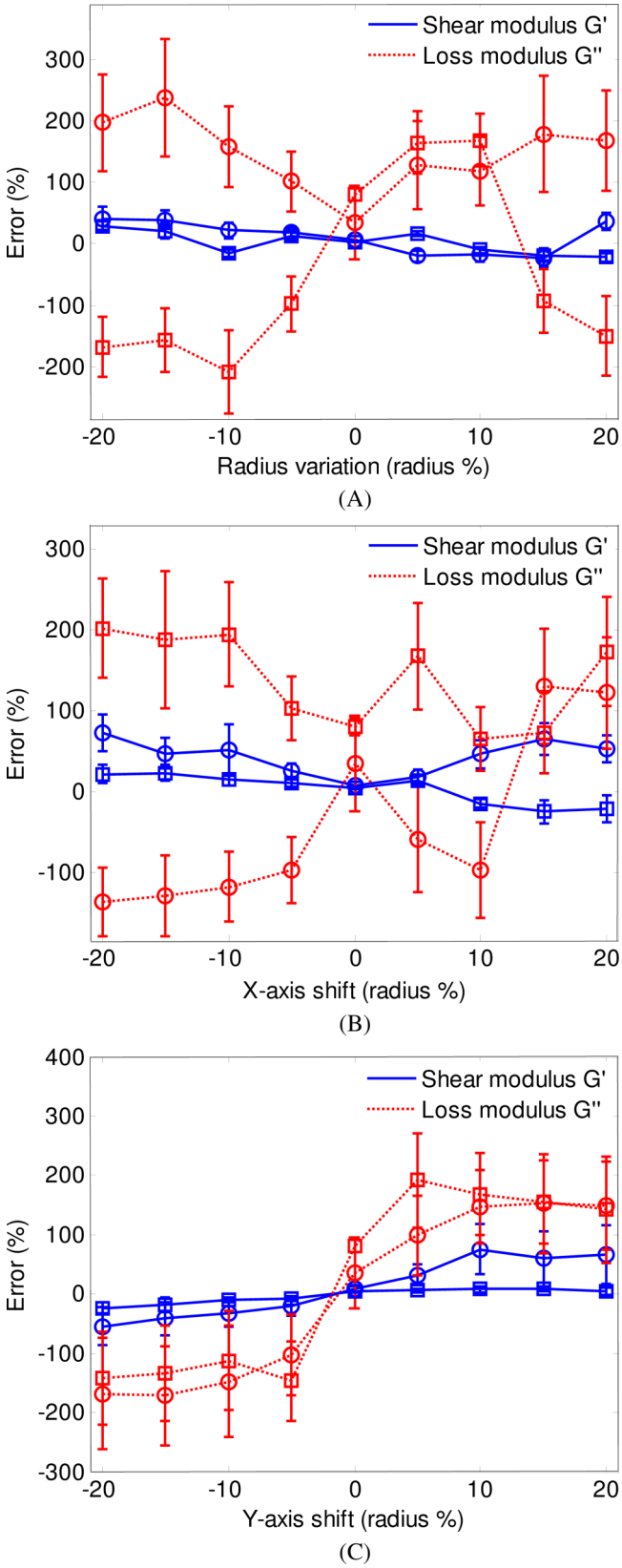

FIG. 6. Errors between predicted finite element method and experimental shear storage (solid blue) and loss (dashed red) moduli for the surrounding medium (squares) and the inclusion (circles) versus (A) the inclusion radius variation, (B) the X-direction shift of the inclusion, and (C) the Y-direction shift of the inclusion in phantom #5. Errors were computed in the frequency range between 40 and 400 Hz. Results are means and standard deviations obtained from ten frequency samples.

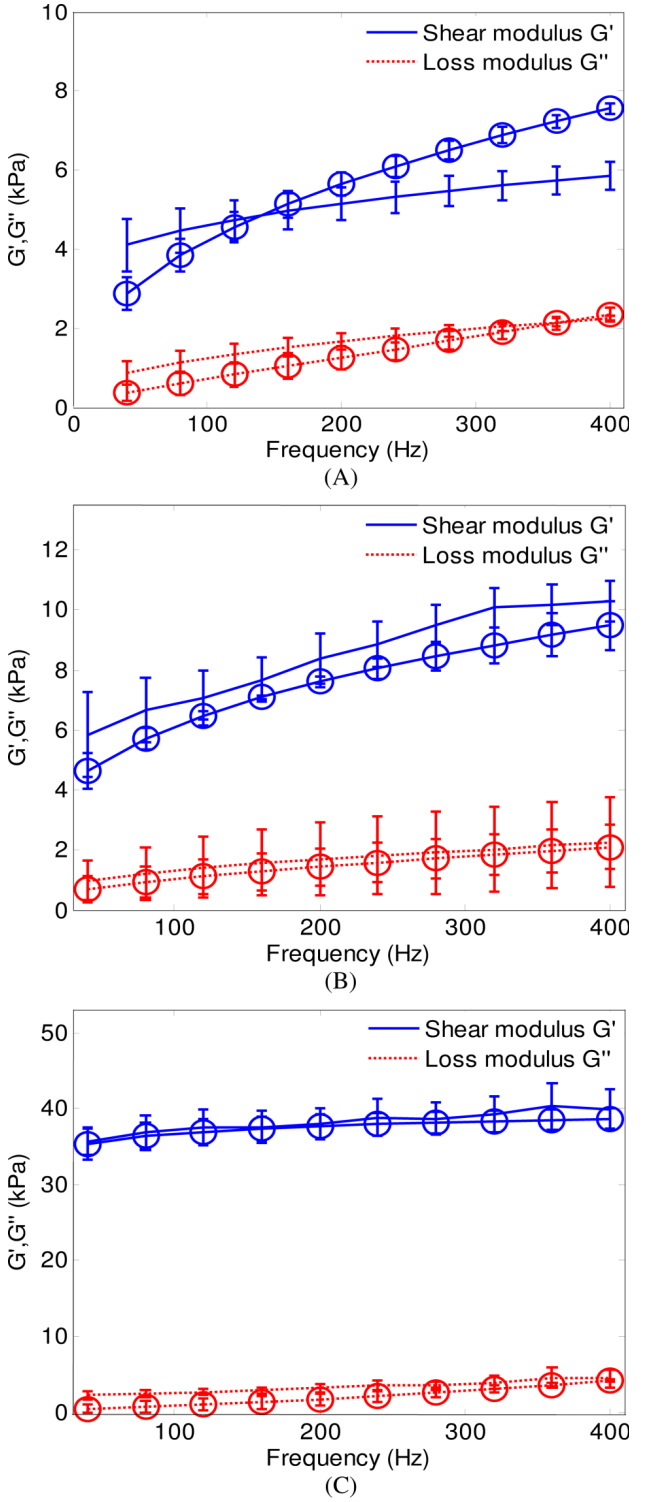

FIG. 7. Shear storage (solid blue) and loss (dashed red) moduli of homogeneous phantoms; (A) phantom #1, (B) phantom #2, and (C) phantom #3, obtained with adaptive torsional shear wave (circles) and benchmark (no symbol) methods. Results represent the mean and standard deviation of three samples (ATSW) and nine samples (benchmark).

modulus, and between 5% and 49% for the loss modulus at frequencies between 120 and 400 Hz. Errors on loss moduli were higher below 120 Hz because benchmark methods reported almost no viscosity.

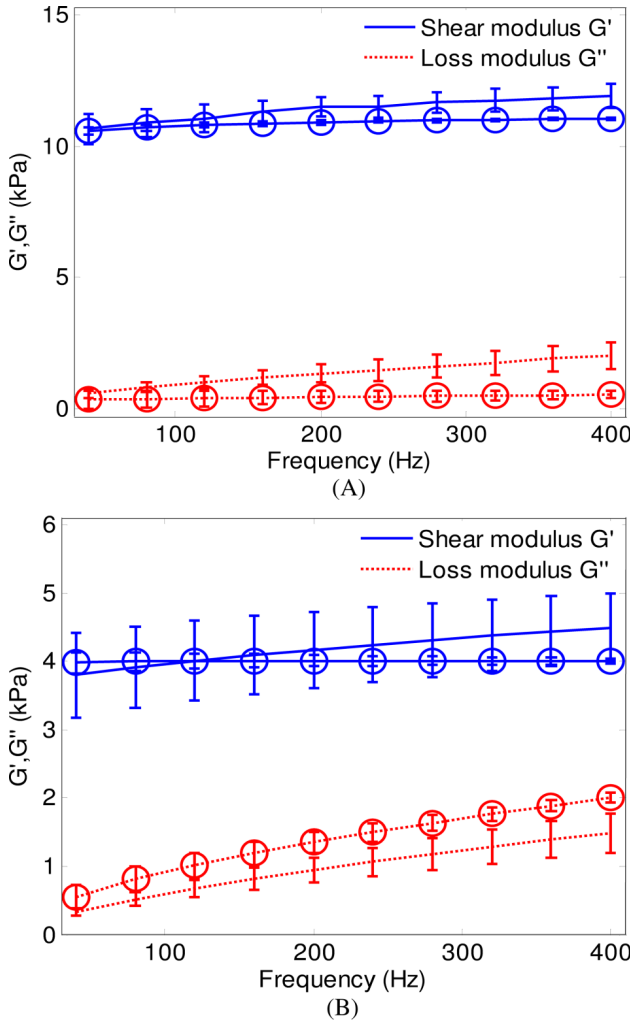

FIG. 8. Shear storage (solid blue) and loss (dashed red) moduli of (A) the surrounding medium and (B) the inclusion of the heterogeneous phantom #4, obtained with adaptive torsional shear wave (circles) and benchmark (no symbol) methods. Results represent the mean and standard deviation of three samples (ATSW) and nine samples (benchmark).

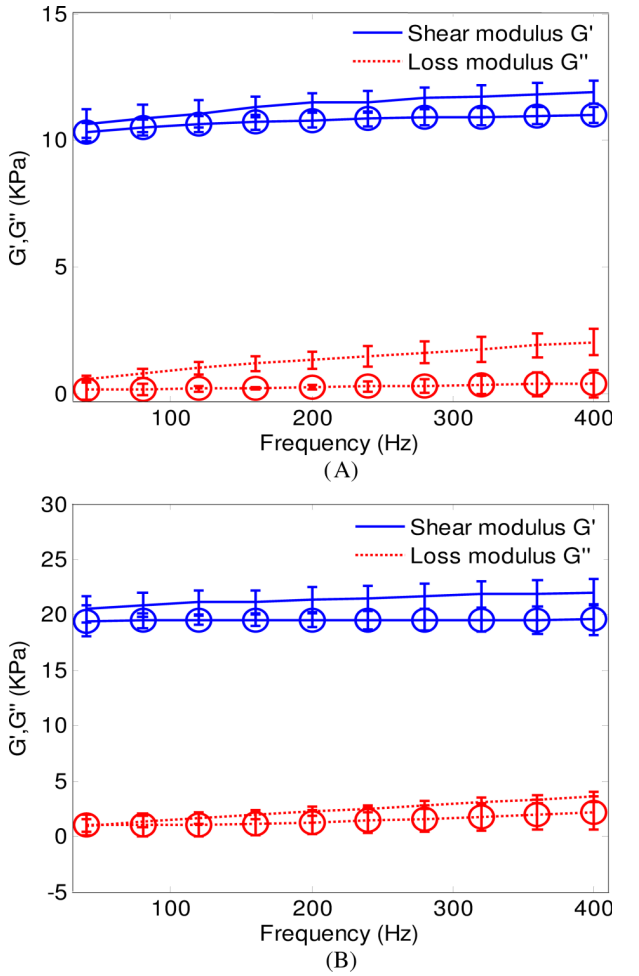

FIG. 9. Shear storage (solid blue) and loss (dashed red) moduli of (A) the surrounding medium and (B) the inclusion of the heterogeneous phantom #5, obtained with adaptive torsional shear wave (circles) and benchmark (no symbol) methods. Results represent the mean and standard deviation of three samples (ATSW) and nine samples (benchmark).

Figures 8 and 9 depict viscoelastic properties of surrounding media and inclusions for heterogeneous phantoms #4 and #5, respectively. In the case of phantom #4, discrepancies with benchmark measures were less than 8% for the storage modulus, and between 23% and 67% for the loss modulus of the surrounding medium, and smaller than 11% for the storage modulus and between 26% and 40% for the loss modulus of the soft inclusion. For phantom #5 (stiff inclusion), errors were similar to those obtained for phantom #4 for the surrounding medium, whereas discrepancies were smaller than 12% and 41% for the storage and loss moduli of the inclusion, respectively.

4. DISCUSSION

4.A. Forward problem validation

As exemplified at 120 Hz in Fig. 3(A) (homogeneous phantom), FEM simulated displacements were in good agreement with experimental profiles between 40 and 400 Hz. For heterogeneous phantoms [see Figs. 3(B) and 3(C) at 120 Hz], correlation coefficients were slightly lower than those of the homogeneous case. As mentioned previously, experimental adaptive torsional shear waves were not generated by eight simultaneous shear wave sources, but reconstructed (in post-processing) from eight individual shear wave sources generated consecutively.[36] Shear wave scattering patterns resulted from the interaction of the shear waves with the inclusion and were slightly different between simulated and experimental cases. Shear wave interferences, which were present in FEM simulations (simultaneous shear wave sources), were not considered in the experimental reconstruction process. This may have influenced the correlation between FEM simulation profiles and experimental ones, which impact was more noticeable for heterogeneous phantoms.

4.B. Robustness study

The robustness study revealed that the proposed inverse problem solution could yield a good estimation of the

storage modulus with relative errors smaller than 19%, even with very noisy signals (SNR = 8.5 dB). Errors were slightly greater for the loss modulus and reached 32% at a SNR of 8.5 dB. In Ref. 25, using a similar inverse problem strategy solved analytically for quasiplane shear waves instead of FEM solutions of torsional waves, errors in the estimation of storage and loss moduli were almost similar (i.e., less than 5% and 42%, respectively), for the same range of SNRs. As the error was estimated for each SNR value at different frequencies (between 40 and 400 Hz) and then averaged, the source of these errors may be the attenuation of shear waves, which is frequency dependent. As the estimation of the shear loss modulus is very sensitive to the attenuation, this latter measure is more affected than the shear storage modulus. Notice that this does not mean that both shear wave polarizations are equivalent dynamic elastography strategies, as previous studies proved the superiority of torsional waves versus quasiplane shear waves to enhance displacements and improve estimation of shear wave velocities.[36] These results signify that considering quasiplane shear waves or torsional waves in the inverse problem provides similar results when fixed noise levels are added to the displacement fields.

For heterogeneous phantoms with a mechanical inclusion, geometry variations of the problem affected viscoelasticity measures, as also observed in Ref. 25. As explained before, the FEM-based inverse problem needs some *a priori* on geometrical parameters (positions X and Y and the radius) due to their impact on the shear wave propagation patterns, which can negatively affect the minimization process and consequently the assessment of the viscoelasticity. However, breast masses can be accurately localized, even the smallest ones with a diameter less than 6 mm,[41,42] which should allow a precise localization of the center of the lesion and reduce X- and Y-direction biases. Furthermore, breast lesions classified in categories BI-RADS 3 and 4 have typically a regular shape and are around 10 mm in diameter when diagnosed.[43,44] Because efficient computerized methods exist to segment breast lesions at ultrasound,[45,46] we believe that the proposed ATSW method is of clinical value as it provides both G' and G'' measurements.

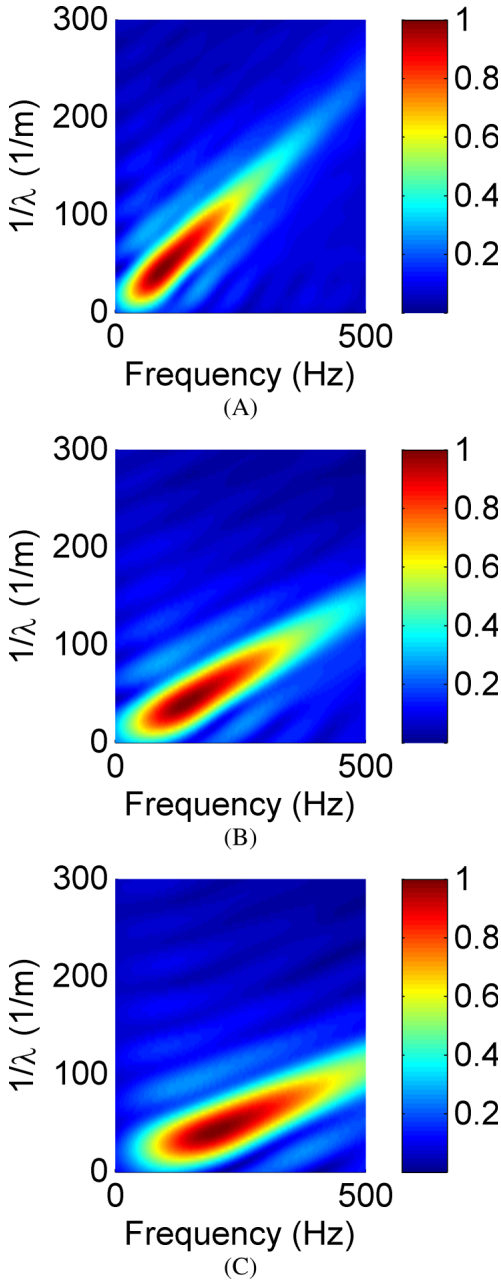

FIG. 10. 2D k-space of normalized displacement fields in homogeneous phantoms: (A) phantom #1, (B) phantom #2, and (C) phantom #3. The maximum amplitude of shear waves was observed between 60 and 150 Hz with a peak at 100 Hz in case of phantom #1, between 100 and 200 Hz with a peak at 150 Hz for phantom #2, and between 150 and 300 Hz with a peak at 200 Hz for phantom #3.

4.C. Viscoelasticity measurements versus benchmark values

For homogeneous phantoms, storage moduli provided by the ATSW method were in very good agreement with benchmark values in frequency ranges of 80–160 Hz for phantom #1, 100–300 Hz for phantom #2, and 150–400 Hz for phantom #3. For phantom #1, results also agreed well with those reported in the literature for similar materials.[7,30,47] Notably, frequency ranges with best agreements between ATSW and benchmark measures correspond to frequency bandwidths where shear wave energies were maximum. This is seen in Fig. 10 displaying 2D wavenumber-frequency (2D k-space) diagrams of displacement fields, as proposed in Ref. 48.

For heterogeneous phantoms, shear storage moduli of surrounding media and inclusions were in good agreement with benchmark methods; however discrepancies were more significant for loss moduli. This may be explained by the small size of inclusions relative to selected wavelength,[49] which affected the estimation of displacements within mimicking lesions and more importantly the estimation of the loss modulus compared to G', as also noticed in Refs. 25 and 49. The frequency range where the proposed method yielded more reliable results generally depended on mechanical properties of propagation media. This range was found to be between 100 and 250 Hz for tested phantoms.

Finally, notice that in a recent study[50] on elasticity estimations of breast lesions using two different shear wave elastography techniques, errors between both methods reached 40%. In our study, when comparing the ATSW method with benchmark G' measures of inclusions, errors were below 11% (we recognize that errors may be larger *in vivo* than with phantom experiments). On the other hand, errors on G'' of inclusions were larger with maximums at 40% for the soft inclusion and 41% for the stiffer one. One may thus conclude that if geometry biases are minimized, the proposed method may allow accurate estimation of elasticity and acceptable assessment of viscosity.

4.D. Summary of limitations

It can be notified that the choice of the benchmark method for future works could be different and based on ultrasound elastography measurements to avoid additional discrepancies due to the physics behind the viscoelasticity assessment. Also, in the actual state, it could be difficult to generate *in vivo* measurements using the proposed method due to the need of using the same probe sequentially. These limitations could be overcome by using a true octagonal probe to avoid using the superposition principle for this proof-of-concept. Indeed, even if FEM simulations demonstrated that there was a very good correlation between ATSW generated simultaneously (true simulated octagonal probe) and those generated sequentially (experimental prototype),[36] the use of a true octagonal probe may change the correlation between experimental and simulated displacement profiles because all interference patterns would be considered, as already explained. This may modify the minimization process of the inverse problem and consequently affect positively or negatively the estimation of the viscoelasticity.

5. CONCLUSION

A new method for the estimation of viscoelasticity was presented in this study. Contrary to a previous study where torsional shear waves were generated by an external oscillating vibrator,[10] the new approach is based on torsional shear waves remotely generated. The proposed method was validated *in vitro* using homogeneous and heterogeneous phantoms through an inverse problem solution, and its robustness to random noise and geometry variations of the problem was evaluated. Shear storage and loss moduli given by the ATSW strategy were found in good agreement with two benchmark rheology methods; discrepancies when present depended on the tested frequency range and mechanical properties of phantoms.

ACKNOWLEDGMENTS

This work was supported by the Natural Sciences and Engineering Research Council of Canada (No. CHRP-365656-09) and by the Canadian Institutes of Health Research (No. CPG-95288). It is now financed by the Fonds Québécois de la Recherche sur la Nature et les Technologies (No. FQRNT-PR-174387). The authors acknowledge Dr. Luc Mongeau for the use of the LWPM technology located in his laboratory at McGill University (Department of Mechanical Engineering).

APPENDIX: BENCHMARK MEASURES

TABLE II. Shear storage (G') and shear loss (G'') moduli of homogeneous phantoms (P #1–#3) obtained using benchmark rheology methods (LWPM and HFVS), and corresponding WMs of nine samples.

			Frequency (Hz)									
			40	80	120	160	200	240	280	320	360	400
P #1	LWPM	G' (kPa)	N/A									
		G'' (kPa)										
	HFVS	G' (kPa)	4.10 ± 0.68	4.47 ± 0.56	4.74 ± 0.50	4.96 ± 0.45	5.15 ± 0.42	5.32 ± 0.40	5.47 ± 0.39	5.61 ± 0.37	5.74 ± 0.36	5.86 ± 0.36
		G'' (kPa)	0.86 ± 0.29	1.14 ± 0.28	1.35 ± 0.25	1.52 ± 0.23	1.67 ± 0.20	1.80 ± 0.17	1.93 ± 0.14	2.05 ± 0.12	2.15 ± 0.09	2.25 ± 0.07
	WM		Same values as HFVS									
P #2	LWPM	G' (kPa)	9.22 ± 0.44	9.36 ± 0.37	9.55 ± 0.37	9.56 ± 0.28	10.1 ± 0.50	10.2 ± 0.49	10.2 ± 0.42	10.3 ± 0.42	10.3 ± 0.53	10.4 ± 0.50
		G'' (kPa)	0.55 ± 0.07	0.57 ± 0.03	0.68 ± 0.04	0.75 ± 0.02	0.76 ± 0.04	0.80 ± 0.03	0.81 ± 0.03	0.88 ± 0.06	10.4 ± 0.05	10.5 ± 0.04
	HFVS	G' (kPa)	3.53 ± 1.40	4.28 ± 1.12	6.44 ± 0.96	6.80 ± 0.86	7.12 ± 0.80	7.40 ± 0.76	8.87 ± 0.75	9.86 ± 0.76	10.1 ± 0.78	10.3 ± 0.81
		G'' (kPa)	1.43 ± 0.71	1.86 ± 0.85	2.17 ± 0.95	2.42 ± 1.02	2.64 ± 1.07	2.83 ± 1.12	3.01 ± 1.16	3.17 ± 1.20	3.32 ± 1.22	3.46 ± 1.25
	WM	G' (kPa)	5.85 ± 1.40	6.67 ± 1.08	7.06 ± 0.92	7.67 ± 0.74	8.38 ± 0.82	8.87 ± 0.76	9.52 ± 0.67	10.1 ± 0.65	10.2 ± 0.68	10.3 ± 0.67
		G'' (kPa)	0.99 ± 0.67	1.22 ± 0.88	1.43 ± 1.01	1.59 ± 1.11	1.70 ± 1.21	1.82 ± 1.29	1.91 ± 1.37	2.03 ± 1.42	2.18 ± 1.43	2.26 ± 1.50
P #3	LWPM	G' (kPa)	36.5 ± 1.67	38.3 ± 1.70	39.1 ± 1.76	38.7 ± 1.96	39.2 ± 1.83	40.6 ± 1.68	39.9 ± 1.83	40.8 ± 1.78	42.8 ± 1.94	41.8 ± 1.89
		G'' (kPa)	2.78 ± 0.09	2.82 ± 0.09	2.98 ± 0.09	3.17 ± 0.10	3.76 ± 0.13	4.10 ± 0.10	3.99 ± 0.14	4.73 ± 0.17	5.89 ± 0.21	5.57 ± 0.21
	HFVS	G' (kPa)	34.8 ± 1.37	35.5 ± 1.48	36.0 ± 1.54	36.4 ± 1.57	36.8 ± 1.59	37.1 ± 1.60	37.3 ± 1.61	37.6 ± 1.62	37.8 ± 1.62	38.0 ± 1.63
		G'' (kPa)	1.68 ± 0.24	2.06 ± 0.20	2.32 ± 0.18	2.53 ± 0.17	2.70 ± 0.17	2.86 ± 0.18	2.99 ± 0.19	3.11 ± 0.21	3.23 ± 0.23	3.33 ± 0.25
	WM	G' (kPa)	35.6 ± 1.76	36.9 ± 2.11	37.6 ± 2.26	37.6 ± 2.10	38.1 ± 2.10	38.8 ± 2.40	38.7 ± 2.16	39.2 ± 2.34	40.3 ± 3.05	40.1 ± 2.60
		G'' (kPa)	2.22 ± 0.58	2.44 ± 0.41	2.65 ± 0.36	2.85 ± 0.35	3.23 ± 0.55	3.48 ± 0.64	3.49 ± 0.53	3.92 ± 0.83	4.56 ± 1.35	4.45 ± 1.14

TABLE III. Shear storage (G') and shear loss (G'') moduli of heterogeneous phantoms (P #4 and #5) obtained using benchmark methods (LWPM and HFVS), and corresponding WMs for surrounding media (sur) and inclusions (inc).

				Frequency (Hz)									
				40	80	120	160	200	240	280	320	360	400
P #4	Sur	LWPM	G' (kPa)	10.0 ± 0.41	10.3 ± 0.45	10.5 ± 0.44	11.0 ± 0.46	11.3 ± 0.46	11.1 ± 0.44	11.3 ± 0.48	11.3 ± 0.51	11.4 ± 0.42	11.5 ± 0.49
			G'' (kPa)	0.61 ± 0.03	0.72 ± 0.03	0.85 ± 0.05	0.94 ± 0.07	0.98 ± 0.06	1.01 ± 0.05	1.11 ± 0.02	1.16 ± 0.05	1.33 ± 0.07	1.38 ± 0.06
	Sur	HFVS	G' (kPa)	10.8 ± 0.87	11.1 ± 0.76	11.2 ± 0.69	11.4 ± 0.63	11.6 ± 0.59	11.7 ± 0.55	11.8 ± 0.53	11.9 ± 0.50	12.0 ± 0.49	12.1 ± 0.48
			G'' (kPa)	0.63 ± 0.68	0.93 ± 0.36	1.18 ± 0.42	1.40 ± 0.47	1.59 ± 0.51	1.77 ± 0.54	1.94 ± 0.57	2.10 ± 0.59	2.33 ± 0.61	2.40 ± 0.63
	Sur	WM	G' (kPa)	10.6 ± 0.58	10.9 ± 0.54	11.1 ± 0.52	11.3 ± 0.41	11.5 ± 0.35	11.5 ± 0.42	11.6 ± 0.40	11.7 ± 0.44	11.8 ± 0.44	11.9 ± 0.45
			G'' (kPa)	0.58 ± 0.14	0.81 ± 0.19	1.01 ± 0.24	1.19 ± 0.28	1.34 ± 0.34	1.47 ± 0.40	1.62 ± 0.43	1.75 ± 0.48	1.91 ± 0.47	2.03 ± 0.52
	Inc	LWPM	G' (kPa)	N/A									
			G'' (kPa)										
	Inc	HFVS	G' (kPa)	3.80 ± 0.62	3.91 ± 0.60	4.01 ± 0.58	4.10 ± 0.57	4.17 ± 0.55	4.24 ± 0.54	4.31 ± 0.53	4.38 ± 0.52	4.44 ± 0.51	4.50 ± 0.50
			G'' (kPa)	0.33 ± 0.06	0.52 ± 0.10	0.68 ± 0.13	0.82 ± 0.16	0.95 ± 0.18	1.06 ± 0.21	1.18 ± 0.23	1.29 ± 0.25	1.39 ± 0.27	1.49 ± 0.30
	Inc	WM	G' (kPa)	Same values as HFVS									
			G'' (kPa)										
P #5	Sur	LWPM	G' (kPa)	10.0 ± 0.41	10.3 ± 0.45	10.5 ± 0.44	11.0 ± 0.46	11.3 ± 0.46	11.1 ± 0.44	11.3 ± 0.48	11.3 ± 0.51	11.4 ± 0.42	11.5 ± 0.49
			G'' (kPa)	0.61 ± 0.03	0.72 ± 0.03	0.85 ± 0.05	0.94 ± 0.07	0.98 ± 0.06	1.01 ± 0.05	1.11 ± 0.02	1.16 ± 0.05	1.33 ± 0.07	1.38 ± 0.06
	Sur	HFVS	G' (kPa)	10.8 ± 0.87	11.1 ± 0.76	11.2 ± 0.69	11.4 ± 0.63	11.6 ± 0.59	11.7 ± 0.55	11.8 ± 0.53	11.9 ± 0.50	12.0 ± 0.49	12.1 ± 0.48
			G'' (kPa)	0.63 ± 0.68	0.93 ± 0.36	1.18 ± 0.42	1.40 ± 0.47	1.59 ± 0.51	1.77 ± 0.54	1.94 ± 0.57	2.10 ± 0.59	2.33 ± 0.61	2.40 ± 0.63
	Sur	WM	G' (kPa)	10.6 ± 0.58	10.9 ± 0.54	11.1 ± 0.52	11.3 ± 0.41	11.5 ± 0.35	11.5 ± 0.42	11.6 ± 0.40	11.7 ± 0.44	11.8 ± 0.44	11.9 ± 0.45
			G'' (kPa)	0.58 ± 0.14	0.81 ± 0.19	1.01 ± 0.24	1.19 ± 0.28	1.34 ± 0.34	1.47 ± 0.40	1.62 ± 0.43	1.75 ± 0.48	1.91 ± 0.47	2.03 ± 0.52
	Inc	LWPM	G' (kPa)	19.7 ± 0.55	20.7 ± 0.71	21.2 ± 0.44	21.2 ± 0.44	21.7 ± 0.72	21.9 ± 0.52	22.4 ± 0.67	22.7 ± 0.67	22.8 ± 0.66	23.0 ± 0.62
			G'' (kPa)	1.63 ± 0.06	1.94 ± 0.05	2.17 ± 0.12	2.36 ± 0.18	2.65 ± 0.15	2.69 ± 0.14	3.01 ± 0.19	3.25 ± 0.07	3.32 ± 0.17	3.40 ± 0.14
	Inc	HFVS	G' (kPa)	20.9 ± 1.26	21.0 ± 1.24	21.1 ± 1.23	21.1 ± 1.22	21.2 ± 1.21	21.3 ± 1.20	21.3 ± 1.18	21.4 ± 1.17	21.5 ± 1.16	21.6 ± 1.15
			G'' (kPa)	0.47 ± 0.07	0.87 ± 0.12	1.26 ± 0.18	1.63 ± 0.23	1.99 ± 0.28	2.35 ± 0.33	2.70 ± 0.38	3.04 ± 0.43	3.38 ± 0.48	3.72 ± 0.52
	Inc	WM	G' (kPa)	20.5 ± 1.23	20.9 ± 1.11	21.1 ± 1.04	21.2 ± 1.03	21.4 ± 1.10	21.5 ± 1.07	21.7 ± 1.15	21.8 ± 1.20	21.9 ± 1.20	22.0 ± 1.22
			G'' (kPa)	0.97 ± 0.58	1.33 ± 0.54	1.65 ± 0.47	1.94 ± 0.42	2.28 ± 0.40	2.50 ± 0.32	2.83 ± 0.35	3.13 ± 0.34	3.36 ± 0.38	3.59 ± 0.43

[a]Now at Rheolution, Inc., Montréal, Québec H2T 1X3, Canada.
[b]Electronic mail: guy.cloutier@umontreal.ca; www.lbum-crchum.com.

[1]K. J. Parker, D. Fu, S. M. Graceswki, F. Yeung, and S. F. Levinson, "Vibration sonoelastography and the detectability of lesions," Ultrasound Med. Biol. **24**, 1437–1447 (1998).
[2]Z. Wu, S. T. Lawrence, D. Rubens, and K. J. Parker, "Sonoelastographic imaging of interference patterns for estimation of the shear velocity of homogeneous biomaterials," Phys. Med. Biol. **49**, 911–922 (2004).
[3]R. M. Lerner, S. R. Huang, and K. J. Parker, "Sonoelasticity images derived from ultrasound signals in mechanically vibrated tissues," Ultrasound Med. Biol. **16**, 231–239 (1990).
[4]M. Fatemi and J. F. Greenleaf, "Vibro-acoustography: An imaging modality based on ultrasound-stimulated acoustic emission," Proc. Natl. Acad. Sci. U. S. A. **96**, 6603–6608 (1999).
[5]L. Sandrin, M. Tanter, J. L. Gennisson, S. Catheline, and M. Fink, "Shear elasticity probe for soft tissues with 1D transient elastography," IEEE Trans. Ultrason., Ferroelectr., Freq. Control **49**, 436–446 (2002).
[6]A. Hadj-Henni, C. Schmitt, and G. Cloutier, "Three-dimensional transient and harmonic shear-wave scattering by a soft cylinder for dynamic vascular elastography," J. Acoust. Soc. Am. **124**, 2394–2405 (2008).
[7]A. Hadj-Henni, C. Schmitt, and G. Cloutier, "Shear wave induced resonance elastography of soft heterogeneous media," J. Biomech. **43**, 1488–1493 (2010).
[8]Q. C. Chan, G. Li, R. L. Ehman, R. C. Grimm, R. Li, and E. S. Yang, "Needle shear wave driver for magnetic resonance elastography," Magn. Reson. Med. **55**(5), 1175–1179 (2006).
[9]C. Schmitt, E. Montagnon, A. Hadj-Henni, S. Qi, and G. Cloutier, "Shear wave induced resonance of venous thrombi: A proof-of-concept," IEEE Trans. Med. Imaging **32**(3), 565–577 (2013).
[10]A. Hadj-Henni, C. Schmitt, I. Trop, and G. Cloutier, "Shear wave induced resonance elastography of spherical masses with polarized torsional waves," Appl. Phys. Lett. **100**, 133702–133705 (2012).
[11]A. P. Sarvazyan, O. V. Rudenko, S. D. Swanson, J. B. Fowlkes, and S. Y. Emelianov, "Shear wave elasticity imaging: New ultrasonic technology of medical diagnostics," Ultrasound Med. Biol. **24**, 1419–1435 (1998).
[12]K. R. Nightingale, M. L. Palmeri, R. W. Nightingale, and G. E. Trahey, "On the feasibility of remote palpation using acoustic radiation force," J. Acoust. Soc. Am. **110**, 625–634 (2001).
[13]M. L. Palmeri, M. H. Wang, J. J. Dahl, K. D. Frinkley, and K. R. Nightingale, "Quantifying hepatic shear modulus *in vivo* using acoustic radiation force," Ultrasound Med. Biol. **34**, 546–558 (2008).
[14]J. Bercoff, M. Tanter, and M. Fink, "Supersonic shear imaging: A new technique for soft tissue elasticity mapping," IEEE Trans. Ultrason., Ferroelectr. Freq. Control **51**, 396–409 (2004).
[15]M. Tanter, J. Bercoff, A. Athanasiou, T. Deffieux, J.-L. Gennisson, G. Montaldo, M. Muller, A. Tardivon, and M. Fink, "Quantitative assessment of breast lesion viscoelasticity: Initial clinical results using supersonic shear imaging," Ultrasound Med. Biol. **34**, 1373–1386 (2008).
[16]S. Chen, M. Fatemi, and J. F. Greenleaf, "Quantifying elasticity and viscosity from measurement of shear wave speed dispersion," J. Acoust. Soc. Am. **115**, 2781–2785 (2004).
[17]K. Nightingale, M. S. Soo, R. Nightingale, and G. Trahey, "Acoustic radiation force impulse imaging: *In vivo* demonstration of clinical feasibility," Ultrasound Med. Biol. **28**, 227–235 (2002).
[18]W. A. Berg, D. O. Cosgrove, C. J. Doré, F. K. W. Schäfer, W. E. Svensson, R. J. Hooley, R. Ohlinger, E. B. Mendelson, C. Balu-Maestro, M. Locatelli, C. Tourasse, B. C. Cavanaugh, V. Juhan, A. T. Stavros, A. Tardivon, J. Gay, J.-P. Henry, and C. Cohen-Bacrie, "Shear wave elastography improves the specificity of breast US: The BE1 multinational study of 939 masses," Radiology **262**, 435–449 (2012).
[19]E. E. Konofagou and K. Hynynen, "Localized harmonic motion imaging: Theory, simulations and experiments," Ultrasound Med. Biol. **29**, 1405–1413 (2003).
[20]C. Shigao, M. Urban, C. Pislaru, R. Kinnick, Z. Yi, Y. Aiping, and J. Greenleaf, "Shearwave dispersion ultrasound vibrometry (SDUV) for measuring tissue elasticity and viscosity," IEEE Trans. Ultrason., Ferroelectr. Freq. Control **56**, 55–62 (2009).
[21]T. Deffieux, G. Montaldo, M. Tanter, and M. Fink, "Shear wave spectroscopy for *in vivo* quantification of human soft tissues visco-elasticity," IEEE Trans. Med. Imaging **28**, 313–322 (2009).

[22]X. Chen, Y. Shen, Y. Zheng, H. Lin, Y. Guo, Y. Zhu, X. Zhang, T. Wang, and S. Chen, "Quantification of liver viscoelasticity with acoustic radiation force: A study of hepatic fibrosis in a rat model," Ultrasound Med. Biol. **39**, 2091–2102 (2013).
[23]S. Chen, W. Sanchez, M. R. Callstrom, B. Gorman, J. T. Lewis, S. O. Sanderson, J. F. Greenleaf, H. Xie, Y. Shi, M. Pashley, V. Shamdasani, M. Lachman, and S. Metz, "Assessment of liver viscoelasticity by using shear waves induced by ultrasound radiation force," Radiology **266**, 964–970 (2013).
[24]M. L. Palmeri, A. C. Sharma, R. R. Bouchard, R. W. Nightingale, and K. R. Nightingale, "A finite-element method model of soft tissue response to impulsive acoustic radiation force," IEEE Trans. Ultrason., Ferroelectr. Freq. Control **52**, 1699–1712 (2005).
[25]E. Montagnon, A. Hadj-Henni, C. Schmitt, and G. Cloutier, "Rheological assessment of a polymeric spherical structure using a three-dimensional shear wave scattering model in dynamic spectroscopy elastography," IEEE Trans. Ultrason., Ferroelectr. Freq. Control **61**, 277–287 (2014).
[26]T. A. Krouskop, T. M. Wheeler, F. Kallel, B. S. Garra, and T. Hall, "Elastic moduli of breast and prostate tissues under compression," Ultrason. Imaging **20**, 260–274 (1998).
[27]D. Cosgrove, W. Berg, C. Doré, D. Skyba, J.-P. Henry, J. Gay, C. Cohen-Bacrie, and TBES Group, "Shear wave elastography for breast masses is highly reproducible," Eur. Radiol. **22**, 1023–1032 (2012).
[28]J. Li, "The effects of menstrual cycle, site and individual variation on breast elasticity and thickness," M.Sc. dissertation, Department of Health Technology and Informatics, The Hong Kong Polytechnic University, 2009.
[29]P. Provenzano, D. Inman, K. Eliceiri, J. Knittel, L. Yan, C. Rueden, J. White, and P. Keely, "Collagen density promotes mammary tumor initiation and progression," BMC Medicine **6**, 11 (2008).
[30]J. L. Gennisson and G. Cloutier, "Sol–gel transition in agar-gelatin mixtures studied with transient elastography," IEEE Trans. Ultrason., Ferroelectr. Freq. Control **53**, 716–723 (2006).
[31]S. Kazemirad, H. K. Heris, and L. Mongeau, "Experimental methods for the characterization of the frequency-dependent viscoelastic properties of soft materials," J. Acoust. Soc. Am. **133**, 3186–3197 (2013).
[32]T. Pritz, "Transfer function method for investigating the complex modulus of acoustic materials: Rod-like specimen," J. Sound Vib. **81**, 359–376 (1982).
[33]A. Hadj-Henni, C. Schmitt, M.-É. Tremblay, M. Hamdine, M.-C. Heuzey, P. Carreau, and G. Cloutier, "Hyper-frequency viscoelastic spectroscopy of biomaterials," J. Mech. Behav. Biomed. Mater. **4**, 1115–1122 (2011).
[34]D. Ekeom, A. Hadj-Henni, and G. Cloutier, "Design of a phased array for the generation of adaptive radiation force along a path surrounding a breast lesion for dynamic ultrasound elastography imaging," IEEE Trans. Ultrason., Ferroelectr. Freq. Control **60**, 552–561 (2013).
[35]A. Ouared, E. Montagnon, S. Kazemirad, L. Gaboury, A. Robidoux, and G. Cloutier, "Frequency adaptation for enhanced radiation force amplitude in dynamic elastography," IEEE Trans. Ultrason., Ferroelectr. Freq. Control **62**, 1453–1466 (2015).
[36]A. Ouared, E. Montagnon, and G. Cloutier, "Generation of remote adaptive torsional shear waves with an octagonal phased array to enhance displacements and reduce variability of shear wave speeds: Comparison with quasi-plane shear wavefronts," Phys. Med. Biol. **60**, 8161–8185 (2015).
[37]M. Fink, "Time reversal of ultrasonic fields. I. Basic principles," IEEE Trans. Ultrason., Ferroelectr. Freq. Control **39**, 555–566 (1992).
[38]E. Montagnon, S. Hissoiny, P. Despres, and G. Cloutier, "Real-time processing in dynamic ultrasound elastography: A GPU-based implementation using CUDA," in *11th International Conference on Information Science, Signal Processing and their Applications, Montreal (ISSPA)* (IEEE, New York, NY, 2012), pp. 472–477.
[39]J. Achenbach, *Wave Propagation in Elastic Solids* (Elsevier Science, New York, NY, 1984).
[40]C. Bacon and J. Pouyet, *Mécanique des Solides Déformables* (Hermes Science, London, 2000).
[41]Q. Zhu, E. B. Cronin, A. A. Currier, H. S. Vine, M. Huang, N. Chen, and C. Xu, "Benign versus malignant breast masses: Optical differentiation with US-guided optical imaging reconstruction," Radiology **237**, 57–66 (2005).
[42]A. Malich, D. Sauner, C. Marx, M. Facius, T. Boehm, S. O. Pfleiderer, M. Fleck, and W. A. Kaiser, "Influence of breast lesion size and histologic findings on tumor detection rate of a computer-aided detection system," Radiology **228**, 851–856 (2003).
[43]S. Raza, S. A. Chikarmane, S. S. Neilsen, L. M. Zorn, and R. L. Birdwell, "BI-RADS 3, 4, and 5 lesions: Value of US in management, follow-up and outcome," Radiology **248**, 773–781 (2008).
[44]M. Nothacker, V. Duda, M. Hahn, M. Warm, F. Degenhardt, H. Madjar, S. Weinbrenner, and U.-S. Albert, "Early detection of breast cancer: Benefits and risks of supplemental breast ultrasound in asymptomatic women with mammographically dense breast tissue. A systematic review," BMC Cancer **9**, 335 (2009).
[45]K. Horsch, M. L. Giger, L. A. Venta, and C. J. Vyborny, "Automatic segmentation of breast lesions on ultrasound," Med. Phys. **28**, 1652–1659 (2001).
[46]A. Madabhushi and D. N. Metaxas, "Combining low-, high-level and empirical domain knowledge for automated segmentation of ultrasonic breast lesions," IEEE Trans. Med. Imaging **22**, 155–169 (2003).
[47]C. Schmitt, A. Hadj-Henni, and G. Cloutier, "Ultrasound dynamic micro-elastography applied to the viscoelastic characterization of soft tissues and arterial walls," Ultrasound Med. Biol. **36**, 1492–1503 (2010).
[48]M. Bernal, I. Nenadic, M. W. Urban, and J. F. Greenleaf, "Material property estimation for tubes and arteries using ultrasound radiation force and analysis of propagating modes," J. Acoust. Soc. Am. **129**, 1344–1354 (2011).
[49]E. Montagnon, A. Hadj-Henni, C. Schmitt, and G. Cloutier, "Viscoelastic characterization of elliptical mechanical heterogeneities using a semi-analytical shear-wave scattering model for elastometry measures," Phys. Med. Biol. **58**, 2325–2348 (2013).
[50]S. Lee, J. Chang, W. Kim, M. Bae, N. Cho, A. Yi, H. Koo, S. Kim, J. Kim, and W. Moon, "Differentiation of benign from malignant solid breast masses: Comparison of two-dimensional and three-dimensional shear-wave elastography," Eur. Radiol. **23**, 1015–1026 (2013).